SURFACE SCIENCE

Optical imaging of surface chemistry and dynamics in confinement

Carlos Macias-Romero, Igor Nahalka, Halil I. Okur, Sylvie Roke*

We imaged the interfacial structure and dynamics of water in a microscopically confined geometry, in three dimensions and on millisecond time scales, with a structurally illuminated wide-field second harmonic microscope. The second harmonic images reported on the orientational order of interfacial water, induced by charge-dipole interactions between water molecules and surface charges. The images were converted into surface potential maps. Spatially resolved surface acid dissociation constant ($pK_{a,s}$) values were determined for the silica deprotonation reaction by following pH-induced chemical changes on the curved and confined surfaces of a glass microcapillary immersed in aqueous solutions. These values ranged from 2.3 to 10.7 along the wall of a single capillary because of surface heterogeneities. Water molecules that rotate along an oscillating external electric field were also imaged.

Microscopic and nanoscopic structural heterogeneities, confinement, and flow critically influence surface chemical processes in electrochemical, geological, and catalytic reactions (*1*–*5*). Recent advances in micro- and nanotechnology are driven by these phenomena, often in combination with electrostatic field gradients that can be surface-intrinsic or externally applied. Micro- and nanocapillaries in combination with interfacial voltage gradients are used in the fabrication, manipulation, and characterization of droplets, interfaces (*6*–*9*), and highly amorphous materials (*10*). An electrostatic field gradient in a narrow channel can be used to separate (*11*) and identify analytes (*12*). The increase in complexity of new materials and nano- and microtechnological developments (*13*) requires technology that can track, in real time, three-dimensional spatial changes in the molecular structure of confined systems, such as curved interfaces and pores, as well as the response to electrostatic fields of these systems.

We have constructed a high-throughput, structured-illumination second harmonic (SH) microscope to perform real-time three-dimensional (3D) chemical imaging of surfaces and confined geometries. Nonresonant coherent SH generation occurs only when noncentrosymmetric molecules, such as water, are oriented noncentrosymmetrically (*14*). This selection rule allows for probing just a few monolayers at an interface. We used this property to image the orientational order of water molecules at the inner and outer surfaces of a glass microcapillary immersed in aqueous solution. The surface chemistry of the microcapillary could be altered by changing the bulk pH of the solution. The images were converted into maps of the surface potential and surface chemical equilibrium constants. Although average values of the surface acid dissociation constant $pK_{a,s}$ agree with previously reported values, structural interfacial heterogeneity was apparent, with $pK_{a,s}$ values ranging locally from 2.3 to 10.7. Dynamical structural changes induced by an external oscillating electrostatic field were also imaged on millisecond time scales and in three dimensions. The observed structural fluctuations at the interface and in the tip opening (diameter <1 μm) originate from water molecules that interact with the external electrostatic field.

The wide-field (*15*–*17*) structured-illumination/HiLo (*18*) SH microscope is shown schematically in Fig. 1A. To achieve the wide-field geometry, we used a cosine diffraction phase grating generated with a spatial light modulator (SLM) to split the illuminating pulsed beam (1036 nm, 200 kHz, 168 fs) into two beams. The SLM was then imaged on the focal (sample) plane of the objectives with the aid of a relay system. The field of view, 150 μm (full width at half maximum), was determined by the spot size on the SLM and the overall magnification of the relay system. The spatial frequency σ of the diffraction grating determined the angle of incidence of the beams on the sample. The image was recorded with an electron-multiplying intensified charge-coupled device (EM-ICCD) camera. Nonlinear polarimetry (*19*) was performed by controlling and analyzing the polarization state of the illuminating and emitted beams. A polarization state generator, comprising a half- and a quarter-wave plate, was used. The polarization state of the emitted light was analyzed with a half-wave plate placed in the emission path, followed by a polarizing beam splitter (*20*).

In a wide-field illumination geometry, 3D imaging is not possible because the beams are too wide. To achieve 3D imaging and to improve the transverse spatial resolution (*21*), we used an adapted HiLo imaging procedure (*18*, *22*–*27*) that relies on partial spatial coherence introduced by a chirp in the illuminating pulse. The procedure is based on Fourier filtering using a cosine intensity pattern containing a carrier spatial frequency to reject out-of-focus light (*20*). With this pattern, structured images I_n and $I_{n'}$ were produced, the latter being phase-shifted by π/2. The processed image was obtained with a uniformly illuminated image ($I_u = I_n + I_{n'}$) and the structured-illumination image (I_n) using a HiLo algorithm (*18*, *23*, *26*–*29*).

We imaged a glass microcapillary immersed in an aqueous solution of pH-neutral ultrapure water with 10 mM NaCl. A phase-contrast image is shown in Fig. 1B; the structured SH images I_n and $I_{n'}$ are shown in Fig. 1, C and D. The uniformly illuminated image obtained from $I_u = I_n + I_{n'}$ is shown in Fig. 1E, and using the algorithm of Mertz and Kim (*27*), we obtained the final HiLo image of Fig. 1F (*20*), where background rejection leads to much better contrast. The corresponding spectrum consisted of a single peak centered at 515 nm (Fig. 1A, left inset), confirming that the image contrast originates from SH emission. The SH intensity was detected in the *XXX* polarization combinations (i.e., with all beams polarized and analyzed in a direction perpendicular to the main symmetry axis of the microcapillary) (Fig. 1C). Light polarized along the interface did not generate SH photons. The measured transverse resolution was 188 nm [Fig. 1A, half width at half maximum (HWHM) of the red curve in the right inset], as measured by imaging $BaTiO_3$ particles 50 nm in diameter (*30*) on a glass coverslip. The best possible axial resolution was 520 nm for two-photon fluorescence (fig. S2) (*20*). The imaging throughput was improved by a factor of ~5×10^3 relative to a scanning confocal two-photon microscope (*31*) and to our previous 2D wide-field SH microscope (*20*, *32*).

Surface chemical changes were SH-imaged and induced on three different glass microcapillaries in solution with pH values of 2, 7, and 12. The ionic strength was kept constant by adding 10 mM NaCl. The silica surface in contact with a solution of pH = 2 is on average charge-neutral, with the vast majority of the silanol groups in the protonated ≡SiOH state (*33*, *34*). Increasing the bulk pH of the solution increased the fraction of surface SiO^- groups, resulting in a predominantly negatively charged surface [with average charge densities of −2 μC/cm² under pH-neutral conditions and < −17 μC/cm² at pH = 12 (*33*, *34*)]. Increasing the net surface charge caused the interfacial electrostatic field E_{DC} to grow in magnitude, and the interaction of this field with the dipole moment of water distorted the orientational distribution of water molecules. The dipole moment of the water molecules aligned with E_{DC}, which allowed SH photons to be generated for probing aqueous silica interfaces (*35*, *36*). Time-averaged and spatially averaged spectroscopic SH measurements have shown that the breaking of centrosymmetry only a few nanometers from the interface is sufficient for generating a detectable SH intensity. The spatially and temporally integrated SH intensity can be correlated to the surface potential Φ_0 according to $I(2\omega) \sim |\chi_s^{(2)} + \chi^{(3)'}\Phi_0 f_3|^2$ (*35*, *37*), which originates from

$$I(2\omega, x, y, t) \sim I(\omega, x, y, t)^2 \left| \chi_s^{(2)}(x, y, t) + \chi^{(3)'} f_3 \int_0^\infty E_{DC}(x, y, z) dz \right|^2 \quad (1)$$

Laboratory for Fundamental BioPhotonics, Institute of Bioengineering, and Institute of Materials Science, School of Engineering, and Lausanne Centre for Ultrafast Science, École Polytechnique Fédérale de Lausanne (EPFL), CH-1015 Lausanne, Switzerland.
*Corresponding author. Email: sylvie.roke@epfl.ch

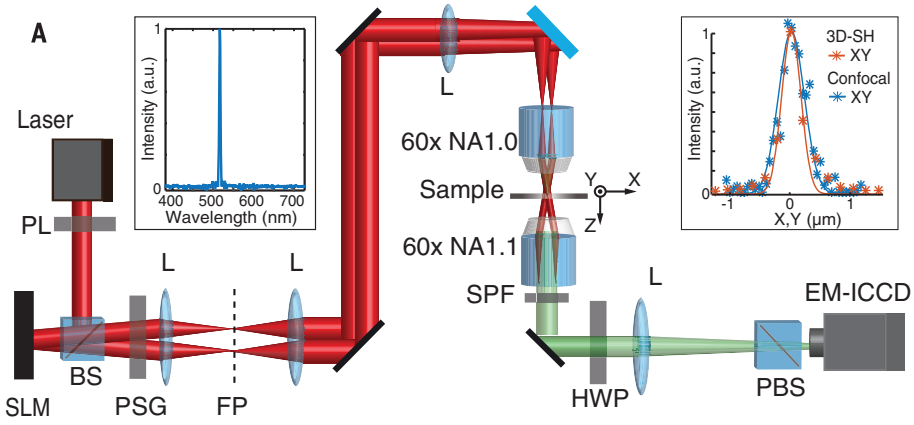

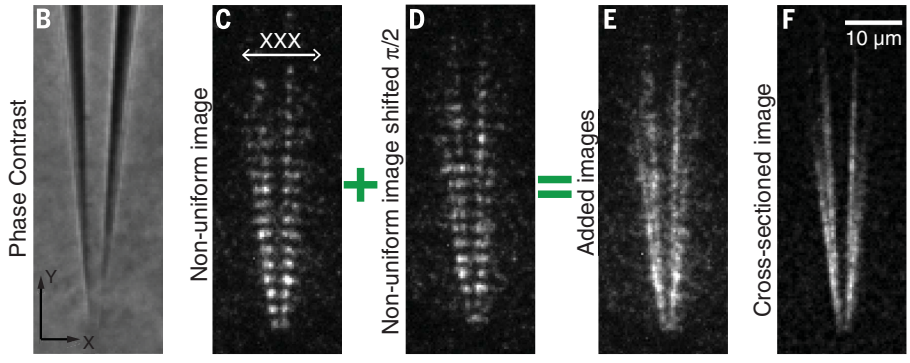

Fig. 1. Optical system and microcapillary imaging. (**A**) Schematic of the 3D second harmonic (SH) microscope. SLM, spatial light modulator; PL, polarizer; BS, beam splitter; PSG, polarization state generator; L, achromatic lens; FP, Fourier plane; NA, numerical aperture; SPF, short pass filter; HWP, half-wave plate; PBS, polarizing BS. Left inset: SH spectrum obtained from the capillary interface. Right inset: Intensity distribution depicting the transverse resolution of the system (red) and that of a commercial scanning multiphoton microscope (blue; Leica SP5, NA 1.2). (**B**) Phase-contrast image of the microcapillary in aqueous solution. (**C** and **D**) SH structured image without (C) and with (D) the pattern phase shifted by $\pi/2$. (**E**) Sum of (C) and (D). (**F**) HiLo image obtained after applying the HiLo algorithm (*27*) on (C) and (E) (*20*). The SH intensity is detectable only if the polarization combination is in the *XXX* direction (i.e., along the surface normal).

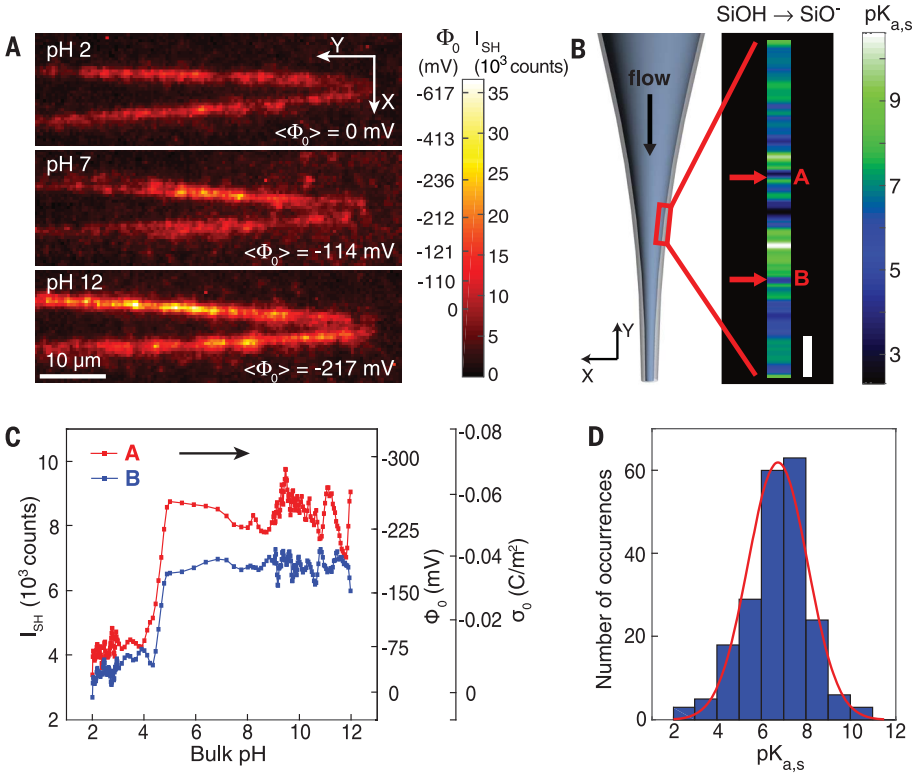

Fig. 2. Imaging of surface chemistry and potential. (**A**) SH cross-sectional images (2 μm thick) using the *XXX* polarization combination for different pH values of the electrolyte solution, recorded with an acquisition time of 5 s per image. The color bar indicates both the intensity I_{SH} and the calculated change in the surface potential Φ_0. (**B**) $pK_{a,s}$ values for the deprotonation reaction of the silica/water interface along the wall of a capillary 100 μm wide, obtained by imaging the change in the surface potential while changing the pH under laminar flow from 2 to 12. The pH is determined using a solution of pH indicator dyes in a separate experiment (*20*). Note that the values are integrated along the *X* direction. Scale bar, 10 μm. (**C**) Change in I_{SH} as a function of pH for two different points labeled in (B), $pK_{a,s}$(A) = 3.8 and $pK_{a,s}$(B) = 5.9. The extracted surface potential and computed surface charge density values are also displayed (*y* axes at right). The arrow indicates the direction of the experiment. (**D**) Histogram of obtained $pK_{a,s}$ values, reflecting the variance in surface reactivity. The red line represents a Gaussian fit.

where *x*, *y*, *z* represents the local surface coordinate system (with *z* being the surface normal), $E_{DC}(x, y, z)$ relates to the electrostatic potential Φ via $-\nabla\Phi(x, y, t)$, $\chi_s^{(2)}$ is the second-order susceptibility of the capillary silica/water surface, and f_3 is an interference term that takes the value 1 for SH transmission experiments (*37*). $\chi^{(3)'}$ is an effective third-order susceptibility that contains different contributions (*20*); the largest is the reorientation of water molecules in the electric double layer [(*37*), here ~99%] (*20*). The response in Eq. 1 can be used to determine changes in the surface potential Φ_0.

The average SH intensity increased in the order pH(2) < pH(neutral) < pH(12), in agreement with

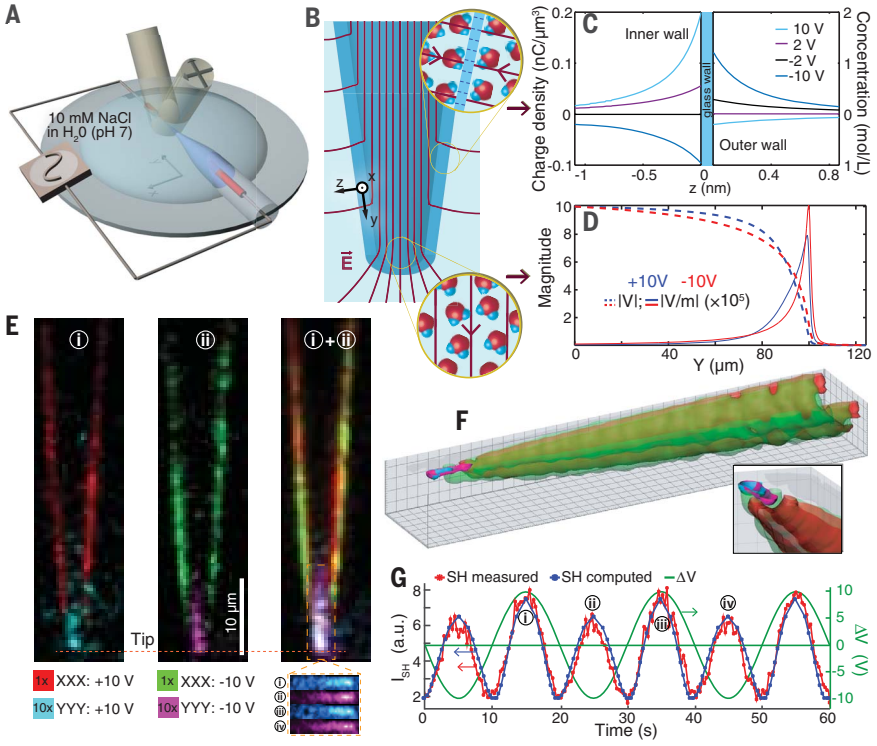

Fig. 3. Dynamic imaging of surface chemical changes. (**A**) Illustration of the experiment. (**B**) Illustration of the applied field lines ($\Delta V > 0$). (**C**) Computed ionic charge density in the aqueous solution adjacent to the interface (fig. S7) (*20*). (**D**) Electrostatic field and potential drop for ΔV = 10 V and ΔV = –10 V along the symmetry (*Y*) axis of the capillary. (**E**) Snapshots of movie S1, recorded with acquisition time of 250 ms for different values of the applied potential (i, 10 V; ii, –10 V; i + ii, composite of five frames each). The ΔV value corresponding to i, ii, iii, and iv is shown in (G). The legend displays the color coding associated with the applied potential, polarization combination, and multiplication factor. The inset at lower right displays the tip region only. All images were normalized with respect to the illuminating beam profile. (**F**) 3D rendering of the 10 V and –10 V channels (45 stacks per 4° rotation around the *Y* axis). The inset shows a zoom-in of the tip. (**G**) ΔV (green), the spatially integrated SH intensity (*XXX* polarization, red), and the numerical computation (blue) (*20*).

expectations from spectroscopic measurements (Fig. 2A) (*35*, *38*–*41*). We converted the SH intensity in the images of Fig. 2A to a change in the surface potential Φ_0. Although it was not possible to determine absolute values for the surface potential in this experiment (*37*), assuming that $\langle\Phi_0\rangle$ = 0 at pH = 2 and that the average charge density under pH-neutral conditions is –2 μC/cm^2 (*33*, *34*), we constructed a scale for Φ_0 using the Gouy-Chapman-Stern model to provide reference values (*34*). The retrieved values are given by the color bar in Fig. 2A. The average values of Φ_0 agree well with reported values (*34*, *38*–*40*). However, the variation in the spatial distribution of intensities/surface potentials was significant, reaching values of ~3$\langle\Phi_0\rangle$. This variation reflected the diverse values reported (*34*, *38*–*40*) and indicated that the surface was structurally not uniform—for example, in terms of the distribution of charged SiO^- or the nanoscopic surface geometry imposed by the production procedure of the capillary (*20*). Indeed, mono-, bi-, or trimodal deprotonation behavior [with surface p$K_{a,s}$ values of 6.8 (*42*), 4.8, 8.5 (*35*), or 3.8, 5.2, and ~9] as well as a dependence on the pH history of the sample (*40*) have been reported. Computations show that the local chemical structure and hydrogen-bonding environment, as well as strains or defects in the surface structures, all contribute to heterogeneity (*43*, *44*).

We determined the spatial distribution of p$K_{a,s}$ values for the $\equiv SiOH_{(s)} + H_2O \rightleftarrows \equiv SiO^-_{(s)} + H_3O^+_{(s)}$ reaction by flowing a pH = 12 solution through a capillary that was charge-neutral on average (Fig. 2, B to D), using a shear rate of 8.5 × 10^3 s^{-1}. We imaged surface potential changes every 250 ms, while the bulk pH changed in the direction of the arrow in Fig. 2C. The pH of the solution was determined with a pH indicator dye solution (*20*) in a separate experiment. Knowing the bulk pH value inside the capillary, we determined the p$K_{a,s}$ value of every pixel according to

$$K_{a,s} = \left[H_3O^+_{(b)}\right]\frac{N_{\equiv SiO^-_{(s)}}}{N_{\equiv SiOH_{(s)}}}\exp\left(-\frac{e\Phi_0}{k_BT}\right)$$
$$\text{and } pK_{a,s} = -\log\left[K_{a,s}\right] \qquad (2)$$

where $N_{\equiv SiO^-_{(s)}}/N_{\equiv SiOH_{(s)}}$ is the ratio of deprotonated over protonated groups, which can be derived from Φ_0 using Gouy-Chapman-Stern theory (*20*, *45*). Figure 2B shows the distribution of p$K_{a,s}$ values for the deprotonation reaction, integrated along the *X* direction. Figure 2C displays the surface potential and derived corresponding surface charge density for two pixels as a function of pH [with p$K_{a,s}$(A) = 3.8 and p$K_{a,s}$(B) = 5.9]. Figure 2D displays histograms of the obtained p$K_{a,s}$ values with an average of 6.7. The chemical reactivity varied spatially from 2.3 < p$K_{a,s}$ < 10.7 and followed a Gaussian distribution. The average value agreed with that in (*42*), but substantial variations in chemical reactivity across the surface were observed, which would explain why different studies [even using the same methods (*35*, *40*)] have found different average p$K_{a,s}$ values.

To image additional types of dynamical changes at interfaces and in confinement, we placed two Ag/AgCl electrodes in a pH-neutral solution that also contained the microcapillary and 10 mM NaCl (Fig. 3A). The electrode outside the capillary was grounded, and the applied electrostatic potential difference ΔV was varied sinusoidally on the inner electrode from 10 V to –10 V at 0.05 Hz (~1 V/s). The spacing between the electrodes was 1 cm, and we imaged the 60-μm-long edge, which had an opening with diameter <1 μm. Solving numerically the Navier-Stokes, Nernst-Planck, and Poisson equations by means of a COMSOL routine, we computed the resulting average changes in E_{DC} as well as the induced flow in the aqueous solution (*20*, *46*) (Fig. 3B). The electrostatic field strength was high (>10^6 V/m) (fig. S9) in the interfacial region and in the tip of the microcapillary. Figure 3C shows the computed average ionic charge density distribution close to the surface for different values of ΔV [using an initial surface charge density of –2 μC/cm^2 (*20*, *33*, *34*)]. As ΔV was cycled from 10 V to –10 V, the electrostatic field at the surface (z = 0) of the microcapillary changed as the distribution of Na^+ and Cl^- ions in the electric double layer changed (fig. S9).

Water molecules that are dynamically oriented by the interfacial DC field can be probed with the *XXX* polarization combination, as in Fig. 2. Another place where the electrostatic field reaches similarly high values is inside the opening of the microcapillary (diameter <1 μm) (*46*). As plotted in Fig. 3D, here E_{DC} oscillates between 0.75 × 10^6 and –1.15 × 10^6 V/m, which corresponds to a fraction of 5 × 10^{-4} oriented water molecules that are fully aligned by it (fig. S4A), or, equivalently, ~1 million aligned water molecules per pixel. These aligned water molecules were probed with the *YYY* polarization combination (i.e., with all beams polarized and analyzed along the main symmetry axis of the capillary).

To image the change in the orientational order of water molecules in both regions as a function of time and applied potential, we recorded 3D SH images (integration time, 250 ms) in different polarization combinations (*XXX* to probe the interfacial water and *YYY* to probe the water in the tip). Movie S1 shows the temporal evolution of the SH intensity. Figure 3E shows 250-ms snapshot cross sections for ΔV = 10 V (i), –10 V (ii), and their composite (averaging 5 frames). The acquisition time, 250 ms, was sufficient to resolve the interfacial water as well as the ~10^6

oriented water molecules in the tip. Figure 3F shows a 3D rendering constructed from 45 image stacks, with each image taken at 4° increments. Movie S2 shows a composite 3D rendering of the oriented water at 10 V (red, cyan) and –10 V (green, purple). There was relatively more oriented water on the inside surface for $\Delta V > 0$ (Fig. 3E, movie S2, and fig. S11), which agrees with the higher E_{DC} there (Fig. 3C and fig. S9). Figure 3G shows the applied potential difference ΔV (green), the spatially averaged SH intensity of the interfacial water (red, *XXX* polarization), and a numerical computation of the intensity using Eq. 1 (blue) (*20*). Good agreement was achieved between the mean-field model and the averaged SH intensity changes. However, the surface response in the images of Fig. 3E (or movie S1) shows that the intensity distribution in the images was not uniform. This difference points toward local variations in the surface structure, potential, and chemical reactivity similar to those observed in Fig. 2 (*20*).

We imaged dynamical interfacial changes as well as small amounts of oriented confined water in three dimensions and on millisecond time scales. The real-time observation of heterogeneous or transient structures should prove valuable for the development of micro- and nanotechnology that critically relies on local structural and dynamical processes (*11*), but also for geochemistry, catalysis, electrochemistry such as in fuel cells (*5*, *11*, *13*, *47*), and processes using electrokinetic phenomena in micro- and nanofluidic environments (*48*). The imaging of the orientational order of water in confinement could be used to noninvasively infer the structure of macromolecules, such as lipids, DNA, and proteins, or structural changes induced by potential gradients.

REFERENCES AND NOTES

1. G. Ertl, H. Knözinger, F. Schüth, J. Weitkamp, *Handbook of Heterogeneous Catalysis* (Wiley-VCH, 2008).
2. J. O. M. Bockris, S. U. Khan, *Surface Electrochemistry: A Molecular Level Approach* (Springer, 2013).
3. B. J. Finlayson-Pitts, J. N. Pitts Jr., *Chemistry of the Upper and Lower Atmosphere: Theory, Experiments, and Applications* (Academic Press, 1999).
4. M. Mrksich, *Curr. Opin. Chem. Biol.* **6**, 794–797 (2002).
5. J. Zachara *et al.*, *Environ. Sci. Technol.* **50**, 2811–2829 (2016).
6. P. J. A. Kenis, R. F. Ismagilov, G. M. Whitesides, *Science* **285**, 83–85 (1999).
7. M. T. Guo, A. Rotem, J. A. Heyman, D. A. Weitz, *Lab Chip* **12**, 2146–2155 (2012).
8. J. C. Baret, F. Mugele, *Phys. Rev. Lett.* **96**, 016106 (2006).
9. F. H. J. van der Heyden, D. Stein, C. Dekker, *Phys. Rev. Lett.* **95**, 116104 (2005).
10. E. Amstad *et al.*, *Science* **349**, 956–960 (2015).
11. R. B. M. Schasfoort, S. Schlautmann, J. Hendrikse, A. van den Berg, *Science* **286**, 942–945 (1999).
12. L. J. Steinbock *et al.*, *J. Phys. Condens. Matter* **22**, 454113 (2010).
13. B. A. Grzybowski, W. T. S. Huck, *Nat. Nanotechnol.* **11**, 585–592 (2016).
14. R. W. Boyd, *Nonlinear Optics* (Academic Press, 2003).
15. M. A. Kriech, J. C. Conboy, *J. Am. Chem. Soc.* **127**, 2834–2835 (2005).
16. M. D. Peterson *et al.*, *Opt. Mater. Express* **1**, 57 (2011).
17. K. Cimatu, S. Baldelli, *J. Am. Chem. Soc.* **130**, 8030–8037 (2008).
18. D. Lim, K. K. Chu, J. Mertz, *Opt. Lett.* **33**, 1819–1821 (2008).
19. E. L. DeWalt *et al.*, *Acta Crystallogr. D* **69**, 74–81 (2013).
20. See supplementary materials.
21. M. G. L. Gustafsson, D. A. Agard, J. W. Sedat, *Proc. SPIE* **3919**, 141–150 (2000).
22. Note that HiLo microscopy is different from HILO (highly inclined and laminated optical) sectioning microscopy.
23. D. Lim, T. N. Ford, K. K. Chu, J. Mertz, *J. Biomed. Opt.* **16**, 016014 (2011).
24. E. Y. S. Yew, C. J. R. Sheppard, P. T. C. So, *Opt. Express* **21**, 12951–12963 (2013).
25. C. Y. Dong *et al.*, *J. Biomed. Opt.* **18**, 031101 (2013).
26. J. Michaelson, H. Choi, P. So, H. Huang, *Biomed. Opt. Express* **3**, 1241–1255 (2012).
27. J. Mertz, J. Kim, *J. Biomed. Opt.* **15**, 016027 (2010).
28. E. Y. S. Yew, H. Choi, D. Kim, P. T. C. So, Wide-field two-photon microscopy with temporal focusing and HiLo background rejection. In *SPIE BiOS* (International Society for Optics and Photonics, 2011), pp. 790310-1–790310-6.
29. S. Santos *et al.*, *J. Biomed. Opt.* **14**, 030502 (2009).
30. C. Macias-Romero *et al.*, *Nano Lett.* **14**, 2552–2557 (2014).
31. E. E. Hoover, J. A. Squier, *Nat. Photonics* **7**, 93–101 (2013).
32. C. Macias-Romero *et al.*, *Opt. Express* **22**, 31102–31112 (2014).
33. J. Sonnefeld, A. Göbel, W. Vogelsberger, *Colloid Polym. Sci.* **273**, 926 (1995).
34. M. A. Brown *et al.*, *Phys. Rev. X* **6**, 011007 (2016).
35. S. Ong, X. Zhao, K. B. Eisenthal, *Chem. Phys. Lett.* **191**, 327–335 (1992).
36. J. M. Gibbs-Davis, J. J. Kruk, C. T. Konek, K. A. Scheidt, F. M. Geiger, *J. Am. Chem. Soc.* **130**, 15444–15447 (2008).
37. G. Gonella, C. Lutgebaucks, A. G. F. de Beer, S. Roke, *J. Phys. Chem. C* **120**, 9165–9173 (2016).
38. C. T. Konek *et al.*, *J. Am. Chem. Soc.* **126**, 11754–11755 (2004).
39. K. C. Jena, P. A. Covert, D. K. Hore, *J. Phys. Chem. Lett.* **2**, 1056–1061 (2011).
40. A. M. Darlington, J. M. Gibbs-Davis, *J. Phys. Chem. C* **119**, 16560–16567 (2015).
41. D. Lis, E. H. Backus, J. Hunger, S. H. Parekh, M. Bonn, *Science* **344**, 1138–1142 (2014).
42. P. von Schindler, H. R. Kamber, *Helv. Chim. Acta* **51**, 1781–1786 (1968).
43. M. Pfeiffer-Laplaud, D. Costa, F. Tielens, M. P. Gaigeot, M. Sulpizi, *J. Phys. Chem. C* **119**, 27354–27362 (2015).
44. K. Leung, I. M. B. Nielsen, L. Criscenti, *J. Am. Chem. Soc.* **131**, 18358–18365 (2009).
45. M. A. Brown, A. Goel, Z. Abbas, *Angew. Chem. Int. Ed.* **55**, 3790–3794 (2016).
46. R. D. Bulushev, S. Marion, A. Radenovic, *Nano Lett.* **15**, 7118–7125 (2015).
47. N. Laohakunakorn *et al.*, *Nano Lett.* **13**, 5141–5146 (2013).
48. T. M. Pearce, J. C. Williams, *Lab Chip* **7**, 30–40 (2007).

ACKNOWLEDGMENTS

We thank S. Caneva for supplying samples and K. F. Domke for discussions. Supported by the Julia Jacobi Foundation, Swiss National Science Foundation grant 200021-146884, European Research Council grant 616305, and the European Union's Horizon 2020 research and innovation program under Marie Skłodowska-Curie grant agreement 721766 (FBI). All data are reported in the main text and supplement. S.R. and C.M.-R. are inventors on patent application US 20150233820 A1 that covers the device and method for measuring and imaging second harmonic and multiphoton-generation scattered radiation.

SUPPLEMENTARY MATERIALS

www.sciencemag.org/content/357/6353/784/suppl/DC1
Materials and Methods
Supplementary Text
Figs. S1 to S12
Movies S1 and S2
References (*49*–*65*)

21 November 2016; resubmitted 5 April 2017
Accepted 30 June 2017
Published online 20 July 2017
10.1126/science.aal4346

Science

Optical imaging of surface chemistry and dynamics in confinement

Carlos Macias-Romero, Igor Nahalka, Halil I. Okur and Sylvie Roke

Science **357** (6353), 784-788.
DOI: 10.1126/science.aal4346originally published online July 20, 2017

Imaging surfaces with water

The surfaces of real materials are often highly chemically heterogeneous, and the reported values of even simple properties such as surface acidity can vary widely in many cases. Macias-Romero *et al.* developed a microscope that images surfaces on the basis of second-harmonic generation from the orientation of interfacial water (see the Perspective by Hunger and Parekh). They followed the deprotonation of silica along glass micropipettes by changing solution pH and found many regions where the surface acidity deviated strongly from the average for the entire micropipette.

Science, this issue p. 784; see also p. 755